Rigid-to-flexible transition in a molecular brush in a good solvent at a semi-dilute concentration

Jia-Jhen Kang,[1,†] Clemens Sachse,[2] Chia-Hsin Ko,[1] Martin A. Schroer,[3,#] Stefano Da Vela,[3] Dmitry Molodenskiy,[3] Joachim Kohlbrecher,[4] Nikita V. Bushuev,[5] Rustam A. Gumerov,[5] Igor I. Potemkin,[5,6] Rainer Jordan[2] and Christine M. Papadakis[1,]*

[1]Fachgebiet Physik weicher Materie, Physik-Department, Technische Universität München, James-Franck-Straße 1, 85748 Garching, Germany

[2]Professur für Makromolekulare Chemie, Fakultät Chemie und Lebensmittelchemie, Technische Universität Dresden, Mommsenstraße 4, 01069 Dresden, Germany

[3]European Molecular Biology Laboratory, Hamburg Outstation, c/o Deutsches Elektronen-Synchrotron, Notkestr. 85, 22607 Hamburg, Germany

[4]Laboratory for Neutron Scattering and Imaging, Paul Scherrer Institut, Forschungsstr. 111, 5232 Villigen PSI, Switzerland

[5]Physics Department, Lomonosov Moscow State University, Moscow 119991, Russian Federation

[6]National Research South Ural State University, Chelyabinsk 454080, Russian Federation

KEYWORDS. molecular brushes, solution behavior, small-angle X-ray scattering, computer simulations, chain conformation

ABSTRACT. The structures of a molecular brush in a good solvent are investigated using synchrotron small-angle X-ray scattering in a wide range of concentrations. The brush under study, P*i*POx$_{239}$-*g*-P*n*PrOx$_{14}$, features a relatively long poly(2-isopropenyl-2-oxazoline) (P*i*POx) backbone and short poly(2-*n*-propyl-2-oxazoline) (P*n*PrOx) side chains. As a solvent, ethanol is used. By model fitting, the overall size and the persistence length as well as the interaction length and interaction strength are determined. At this, the interplay between form and structure factor is taken into account. The conformation of the molecular brush is traced upon increasing the solution concentration, and a rigid-to-flexible transition is found near the overlap concentration. Finally, the results of computer simulations of the molecular brush solutions confirm the experimental results.

Introduction

Molecular brushes (MBs) are composed of a backbone, which is densely grafted by a large number of polymeric side chains, also called "bottle brushes".[1,2,3,4] Due to the high grafting density, the steric hindrance between the side chains results in a high stiffness of the backbone, compared to the corresponding bare linear polymers, and a stretched conformation of both the backbone and the side chains. The architecture of MBs is characterized by the degree of polymerization of the backbone, N_{bk}, the degree of polymerization of the side chains, N_{sc}, and the grafting density, z, defined as the number of side chains grafted per each backbone monomer. z is generally larger than 0.5.

Changing the relative length ratio between the backbone and the side chains leads to various molecular structures.[5,6,7] When the side chains are much longer than the backbone, the MB has a structure close to the one of a star-like polymer and therefore assumes a spherical or ellipsoidal shape. In contrast, when the backbone is significantly longer than the side chains, the MB resembles a large worm-like chain. Numerous studies have addressed the relation between the architectural parameters and the conformation of MBs, both theoretically,[8,9] in simulations[10,11,12,13,14,15,16,17,18,19] and experimentally.[20,21,22,23]

Since the structure of MBs resembles the one of a large linear polymer chain with a finite cross section,[24,25,26] especially for MBs with long backbone, they may be considered as worm-like chains having a contour length L_c, a persistence length l_p and a cross-sectional radius R_c. These quantities can be estimated theoretically[27] or can be experimentally determined using small-angle X-ray or neutron scattering.[22,28,29]

The theoretical work by Borisov et al. addressed the relation between the end-to-end distance R_{ee} of MBs and the solution concentration c, from the dilute to the concentrated regime.[8] In this study, a number of parameters are considered, including the solvent quality for the backbone and the side chains, the molar masses of the backbone and the side chains, and the grafting density of the MB. In dilute solution, the MBs were found assume their unperturbed conformation, which stays unchanged with increasing concentration, until the overlap concentration c^* is reached. Above c^*, the mutual interaction affects the conformation of the MBs, and quantitative scaling laws between R_{ee} and c were predicted, where the length scale of the mutual interaction decreases with increasing concentration. When the solvent quality is good for both, the backbone and the side chains, right above c^*, the interaction between the backbones dominates, and the scaling relation $R_{ee} \propto c^{-0.125}$ was identified, i.e. the same as for linear polymers in solution. Upon further

increasing the concentration, the interaction between the side chains dominates, and a scaling relation of $R_{ee} \propto c^{-0.304}$ was predicted for this second regime. When the length scale of the mutual interaction decreases to the level of the local segmental lengths, first to the persistence length l_p and then the cross-sectional radius R_c, these are both predicted to depend on concentration. Thus, in the second interaction regime, the rigidity of the backbone and the side chains gradually decreases with increasing concentration. Finally, for the highest concentrations, R_{ee} is not concentration-dependent, with both the backbone and the side chains featuring Gaussian conformation.

In the simulation study by Paturej and Kreer, similar findings as in the described theoretical work[8] were reported, with a detailed description on the different regimes of mutual interactions between MBs in good solvent.[17] Four interaction regimes were identified above the overlap concentration $c^* = c_1$: (1) the backbone interaction regime, yielding $R_{ee} \propto c^{-0.125}$, (2) the persistence length interaction regime, yielding $R_{ee} \propto c^{-0.25}$, (3) the inter-side chain interaction regime, yielding $R_{ee} \propto c^{-0.308}$ and (4) the inter- and intra- side chain interaction regime, yielding $R_{ee} \propto c^{-0.4}$. In regimes (3) and (4), the term "inter-" refers to the interaction between side chains from adjacent MBs, while the term "intra-" refers to the interaction between side chains belonging to the same MB. In the same work, the role of the architectural parameters, i.e., N_{sc} and z, on the relation between R_{ee} and c was demonstrated by several examples.[17] In the extreme case of $N_{sc} = 1$, the concentration dependence of R_{ee} shows the behavior of regime (1) followed immediately by regime (2), which lasts to higher concentrations. This means, no interaction between the side chains is observed in this case, presumably due to the very short side chain length. In contrast, when z is set to 2 and N_{sc} to 16, the concentration dependence of R_{ee} shows the behavior of regime (1) directly followed by regime (4), while regimes (2) and (3) are not observed. This direct cross-over was

explained by the high grafting density combined with the long side chains, resulting in a dominance of the side chain interactions between the MBs. These simulation results show that the occurrence of the interaction regimes depends strongly on the MB architecture.

As for experimental studies, the MB conformation could be characterized in dilute solution using small-angle scattering, and relations between the architectural parameters and the conformation were identified.[20,21,23,30,31,32] Typically, the MBs were modeled as flexible cylinders, giving the structural parameters L_c, l_p and R_c. In contrast, the concentration dependence of the MBs' chain conformation and inner structure was much less studied. At this, one of the challenges arises from modeling of the data, since the data in semi-dilute solutions are characterized by an interplay of numerous length scales, including the ones within the MBs as well as the correlation lengths between the MBs, making it difficult to determine the parameters unambiguously.[33] Another challenge is to describe the contribution of the mutual interaction properly. As indicated by theoretical and simulation studies, the conformation of individual MBs is expected to change with polymer concentration in semi-dilute solutions, and their correlation may depend on the actual conformation. This interplay of form and structure factor has, to the best of our knowledge, not been considered yet.

In the work by Bolisetty et al., the conformation of a long MB (N_{bk} = 1600, N_{sc} = 61) was characterized from dilute to semi-dilute solution in a good solvent,[34,35] using small-angle neutron scattering (SANS). The scattering of the MBs was modeled as a flexible cylinder form factor. The mutual interaction was described by a virial series in c, which had proven applicable for, among others, dendrimers.[36,37,38] Despite the limited number of data points, the radius of gyration, R_g, of the MBs was found to follow the theoretical prediction by Borisov et al., showing firstly $R_g \propto c^{-0.125}$ (backbone interaction dominant) and subsequently $R_g \propto c^{-0.304}$ (side chain interaction

dominant) with increasing solution concentration, i.e. the first and the second regimes. Meanwhile, the persistence length l_p of the MBs decreases steadily with increasing concentration, implying a decreasing stiffness of the backbone.

Sunday et al. also investigated the scaling relation between R_g and c of a MB (N_{bk} = 105 and N_{sc} = 40) in a good solvent using SANS, covering a broad range of concentration.[39] To avoid ambiguities due to the overlapping length scales during the data analysis, the data were described by the generalized Guinier-Porod model instead of assigning a specific shape. This protocol allowed a precise determination of the radii of gyration in the longitudinal ($R_{g,2}$) and the perpendicular direction ($R_{g,1}$) of the anisotropic MBs; however, the detailed structural features were not provided. From these, values of the overall R_g and the persistence length l_p were calculated. As for the mutual interaction between MBs, the Percus-Yevick hard-sphere structure factor was used, which is the simplest correlation model for interacting particles. This way, from dilute to semi-dilute condition, three interaction regimes could be identified, namely $R_g \propto c^{-0.11}$, $R_g \propto c^{-0.35}$ and $R_g \propto c^{-0.10}$. These exponents slightly differ from the ones identified experimentally by Bolisetty et al.[34,35] and theoretically by Paturej and Kreer.[17] Evaluating the concentration dependence of $R_{g,2}/R_{g,1}$, it was found that the overall shape of the MBs becomes less anisotropic upon increasing concentration, which corresponds well to the decreasing rigidity of the backbone at high concentrations found by Bolisetty et al.[34,35]

Although a number of experimental investigations have addressed the concentration dependence of the conformation of MBs, the idea, that the mutual interaction between MBs may depend on the conformation of individual MBs, has not yet been pursued in the analysis of small-angle scattering data. For a proper description, the scattering contribution from the MB interaction should include the conformational information on the individual MBs, which is absent in the previous modelling

approaches, in the fitting model in order to account for the conformational evolution upon variation of the concentration in the solution. In addition, we performed mesoscopic computer simulations of the molecular brush solutions in order to confirm the experimental data.

Experimental

Polymer Characteristics

The MB under study, P*i*POx$_{239}$-*g*-P*n*PrOx$_{14}$, features a poly(2-isopropenyl-2-oxazoline) (P*i*POx) backbone and poly(2-*n*-propyl-2-oxazoline) (P*n*PrOx) side chains, having degrees of polymerization of N_{bk} = 239 and N_{sc} = 14, respectively (Figure 1). The grafting-from method was used to synthesize the MB according to a modified method based on ref 40, also described in ref 41. At this, the backbone was synthesized by living anionic polymerization of 2-isopropenyl-2-oxazoline, which was further converted to a macroinitiator salt by reaction with methyl triflate. From this macroinitiator salt, the side chain was grafted by living cationic ring-opening polymerization. The grafting reaction was terminated with *N*-Boc-piperazine to improve end group analysis by ^{1}H-NMR. As determined by the refractive index detection of size exclusion chromatography (SEC), the weight-average molar mass of the backbone, $M_{w,bk}$, is 29.4 kg mol^{-1} with a polydispersity $Đ$ = 1.09. For the whole MB, the weight-average molar mass, M_w is 413.1 kg mol^{-1} with $Đ$ = 1.01, as determined by SEC multi-angle laser light scattering detection and 141.3 kg mol^{-1} with $Đ$ = 1.12 by refractive index detection. Both elugrams are given in Figure S1 in the Supporting Information (SI).

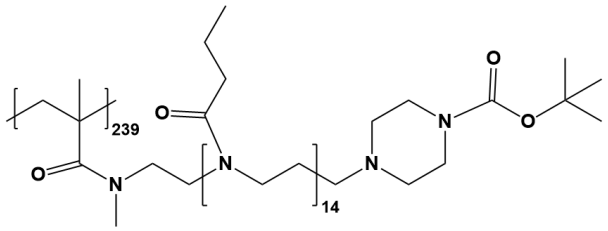

Figure 1. Chemical structure of P*i*POx$_{239}$-*g*-P*n*PrOx$_{14}$

SEC measurements were performed on a system from Jasco (Groß-Umstadt, Germany) with a PU 2080 HPLC-pump, a JetStream II Plus column oven, equipped with one Gram 3000 8 × 300 mm and one Gram 30 8 × 300 mm column and dimethylacetamide (DMAc) with 5 g L^{-1} LiBr and 1 vol% H_2O as the mobile phase at 70 °C. The system was calibrated with PMMA standards (PSS, Mainz, Germany). A Dawn DSP-laser photometer at λ = 632.8 nm (Wyatt Technology, Dernbach, Germany) and an RI-930 RI detector (Jasco) were used for detection. Samples were dissolved in the mobile phase and filtered through 0.2 µm PTFE syringe filters prior to the measurement. Refractive index increments d*n*/d*c* were determined using a differential refractometer DR1/b from SLS Systemtechnik (Denzlingen, Germany) in the concentration range of 1–5 g L^{-1} at a temperature of 35 °C.

Sample Preparation

For sample preparation, ethanol (99.8 %, ROTIPURAN®) or perdeuterated ethanol-d_6 (99.0 %, Deutero GmbH, Kastellaun, Germany) were filtered using mixed cellulose ester membrane syringe filters having a pore size of 0.8 µm. Polymer solutions having polymer concentrations *c* = 5, 20, 30 and 46 g L^{-1} were prepared in ethanol and in ethanol-d_6 for *c* = 1.25, 2,5 and 10 g L^{-1}. Ethanol-d_6 was chosen to enable comparison with small-angle neutron scattering data from previous experiments. No difference was found in the SAXS data from solutions in ethanol or ethanol-d_6,

see below. In each series, the most concentrated solution was prepared first and was diluted to the desired concentration. The solutions were placed on a shaker for at least two weeks before the measurements.

Synchrotron Small-angle X-ray Scattering

SAXS measurements were conducted at the high brilliance synchrotron SAXS beamline P12 at the Deutsches Elektronen Synchrotron (DESY), Hamburg, Germany.[42] The employed wavelength of the X-rays was $\lambda = 0.124$ nm, and the sample-to-detector distance (SDD) was 3.0 m, together providing a q-range of 0.03 – 4.5 nm^{-1}, where $q = 4\pi \times \sin(\theta/2)/\lambda$ is the momentum transfer with θ being the scattering angle. The 2D Pilatus 6M detector was used, recording the scattering as 2D intensity pattern. The illumination time for each measurement was 45 ms. The sample temperature was 20 °C. During data acquisition, the solution flowed continuously through a thermo-controlled capillary (50 μm in wall thickness and 1.7 mm in inner diameter) for X-ray illumination, using a robotic sample changer to avoid the chance of radiation damage.[43,44] 20 measurements were carried out in sequence, and the averaged data were taken, which were corrected by the transmission and brought to absolute scale using water as a standard. After azimuthal averaging of the 2D intensity, the 1D SAXS data of the solvent was subtracted. These operations were carried out by the automated data processing pipeline SASFLOW.[45]

Data Analysis

From the scattered intensity profile $I(q)$, pair distance distribution functions $p(r)$ were calculated to obtain model-free information on the shape and inner structure of the MBs as well as their maximum size r_{max} and their radius of gyration, R_g, and to identify possible correlations between

the MBs.[46] For the calculation of $p(r)$ and R_g, the program GNOM was used.[47] Additionally, *ab initio* shape modeling of the $P_{fc}(q)$ curves for 1.25, 10 and 46 g L^{-1} was carried out with the program DAMMIF.[48] In detail, for each data set, 10 reconstructions were generated in slow mode, and the resulting models were clustered using the program DAMCLUST.[49] The stability of the reconstructions was quantified in terms of the Normalized Spatial Discrepancy (NSD).[50] This metric exceeds a value of 1, when the models differ systematically from each other. After clustering the *ab initio* shape models, a representative model of the largest cluster, as determined by DAMCLUST, for each of the three concentrations was selected. All programs are implemented in the software ATSAS 3.0.[51] For the calculation of $p(r)$, the q-range 0.04 – 1.14 nm^{-1} was selected.

The shape of $p(r)$ provides indication about the structure of the molecular brushes, which is taken into consideration when choosing the model for analyzing the SAXS data. For dilute solutions, i.e., c = 1.25-5 g L^{-1}, the following model was chosen:

$$I(q) = P_{fc}(q) + I_{bk} \quad (1)$$

where $P_{fc}(q)$ is the flexible cylinder form factor with a polydisperse cross-sectional radius, describing the individual MB (Figure S2 and eqs S1 and S2 in the SI) and I_{bk} a constant background.[52,53] As the degree of polymerization of the backbone is much larger than the one of the side chains, it is expected to resemble a semi-flexible polymer chain with a finite cross section. From $P_{fc}(q)$, the contour length L_c, the persistence length l_p and the cross-sectional radius R_c of the MB are obtained. An exemplary fit is shown in Figure S3a in the SI.

As for the semi-dilute solutions, i.e., 10-46 g L^{-1}, the contribution from the interaction between the MBs and the chain scattering were included in the fitting model:

$$I(q) = P_{fc}(q)S_{wlc}(q) + I_{fluct}(q) + I_{bk} \quad (2)$$

$S_{wlc}(q)$ is the structure factor describing the interaction between worm-like chains (eqs S3-S6 in the SI), and $I_{fluct}(q)$ is the scattering from the local concentration fluctuations (eq S7 in the SI).

$S_{wlc}(q)$ accounts for the correlations between the chain-like MBs, giving the interaction factor β, and a characteristic interaction length L_{int}. $S_{wlc}(q)$ is an explicit function of $P_{fc}(q)$ (eq S3 in the SI) and is therefore dependent on the MB conformation.[52, 54] The contribution from the local concentration fluctuation, $I_{fluct}(q)$, was described by the Ornstein-Zernike structure factor.[55] It accounts mainly for the scattering from the side chains, giving the correlation length ξ of the concentration fluctuations. Figure S3b in the SI demonstrates the contributions from each term in eq 2 to the model fit.

The procedure for fitting was the following: (1) We fitted the 1.25 g L^{-1} data with all parameters being free fitting parameters. This way, the contour length of the molecular brush was obtained. (2) This value of the contour length was fixed, when the data for the concentrations 2.5 - 46 g L^{-1} were fitted. The background scattering was taken as a free fitting parameter for 1.25 – 5 g L^{-1}, while it was fixed at 2.36×10^{-4} cm^2 g^{-1} for 10 – 46 g L^{-1}. I_{bk} was taken as a free fitting parameter for the dilute solutions, i.e., 1.25 – 5 g L^{-1}, while it was fixed at 2.36×10^{-4} cm^2 g^{-1} for the semi-dilute solutions, i.e., 10 – 46 g L^{-1}. For model fitting, the software SASfit 0.94.12 was used.[56] The resulting structural parameters are given in Table S1 in the SI. The uncertainties shown are the ones given by this software. Confidence intervals are given in the SI.

Results

Overview

SAXS measurements were performed on P*i*POx$_{239}$-*g*-P*n*PrOx$_{14}$ solutions at 20 °C in a concentration range c = 1.25-46 g L^{-1} (Figure 2). No difference is observed for solutions in ethanol and ethanol-d6. The SAXS data of the most dilute sample, i.e., 1.25 g L^{-1}, show the typical features of worm-like particles: in the low q range (q < 0.08 nm^{-1}), reflecting structures at large length scales, the scattering intensity $I(q)$ reaches a plateau, as it is for dilute homogeneous particles whose size can be well-defined in the given q-range. Its absolute value is related to the contour length of the MB, L_c.

At intermediate q-values (0.1-0.5 nm^{-1}), a decay following $I(q) \propto q^{-5/3}$ is observed, characteristic of the scattering from a worm-like chain having a persistence length l_p.[57] The cross-over position from the plateau to $q^{-5/3}$ marks the overall size of the MBs. Further, at 0.7-1.5 nm^{-1}, $I(q)$ shows a decay $I(q) \propto q^{-4}$, which results from the sharp cross section of the MBs, that is due to the densely grafted side chains on the backbone. The q-value, at which the cross-over between these two relations occurs, is related to l_p. The cross-over between the q^{-4} behavior and the subsequent, weaker dependence is related to the cross-sectional radius of the MB, R_c. At q > 1.5 nm^{-1}, $I(q)$ is independent of q, which is considered as the background scattering.

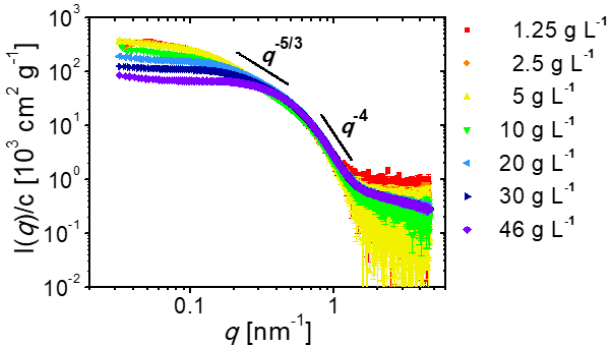

Figure 2. Concentration-normalized SAXS data $I(q)/c$ (symbols) of the P*i*POx$_{239}$-*g*-P*n*PrOx$_{14}$ solutions at 20 °C in ethanol for the concentrations given in the legend. The lines indicate the power laws $I(q) \sim q^{-5/3}$ and $I(q) \sim q^{-4}$.

From 1.25 g L^{-1} up to 5 g L^{-1}, the normalized scattering intensity $I(q)/c$ stays nearly unchanged (Figure 2). Shifted curves are given in Figure 3 for better visibility. It is noted that the curves are similar, regard less of whether ethanol or ethanol-d$_6$ was used as a solvent. Above 5 g L^{-1}, the intensity at low q values (< ~0.2 nm^{-1}) is successively suppressed with increasing concentration. Furthermore, the range over which the behavior $I(q) \propto q^{-5/3}$ is observed, diminishes with increasing concentration, implying a decrease in the persistence length l_p. In the range 0.7-1.5 nm^{-1}, the SAXS data overlap for all concentrations, indicating a constant cross-sectional radius R_c. In the highest q range, namely q > 1.5 nm^{-1}, $I(q)/c$ is independent of q for 1.25-5 g L^{-1}, while a shallow decay of $I(q)/c$ is observed for 10-46 g L^{-1}. This decay is attributed to the concentration fluctuations at small length scales, which are presumably caused by the side chain scattering and are only detectable, when the concentration and thus the scattering intensity is high enough. In the high-q range, the data for 10-46 g L^{-1} overlap very well, suggesting that the scattering from the side chains hardly depends on concentration in this range. The SAXS data along with the model fits are also shown as Kratky plots in Figure S4 in the SI. They confirm that the fits are excellent in the entire q-range.

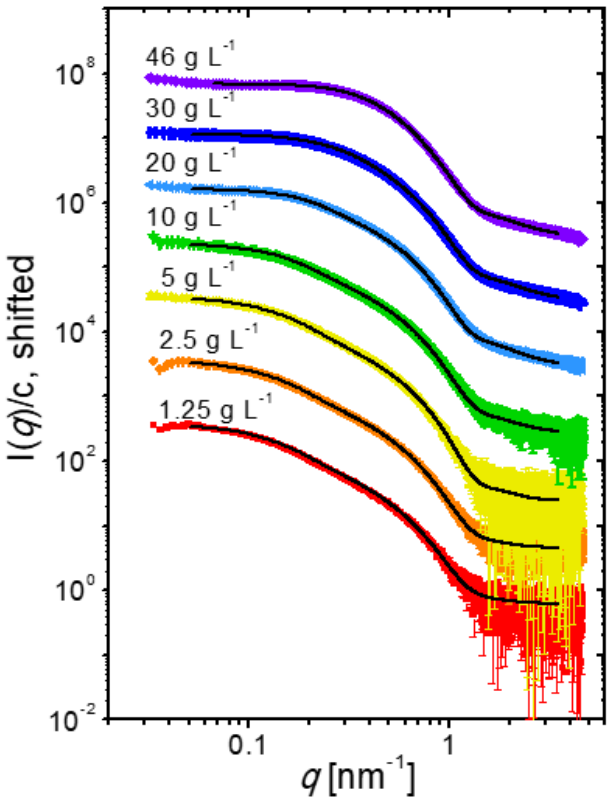

Figure 3. SAXS data (symbols) together with the model fits (solid lines, see text). The concentrations are indicated in the graphs. The data are vertically shifted by a factor of 10 with respect to each other for better visibility.

From the SAXS data, the pair distance distribution functions, $p(r)$, are derived (Figure 4), giving hints to the overall shape of the MBs as well as their correlation in dependence on concentration. The $p(r)$ function of the most dilute sample (c = 1.25 g L^{-1}) is asymmetric. It shows two maxima at the distances r = 5 nm and r = 11 nm and a steady decay between r = 11 and 47 nm. The latter represents the maximum dimension in the MB, r_{max}. Upon increasing the concentration to 10 g L^{-1}, the $p(r)$ function stays overall asymmetric, and the maximum at r = 5 nm is unchanged, while the one at r = 11 nm becomes shallower and nearly disappears. Meanwhile, the decay at r > 11 nm gradually shifts toward lower r-values by ~3-5 nm, i.e. r_{max} shrinks slightly. Thus, in the

concentration range of 1.25-10 g L^{-1}, the MBs feature an anisotropic shape with two inherent length scales, which shall be disclosed by the interpretation of the model fitting results of $I(q)$.

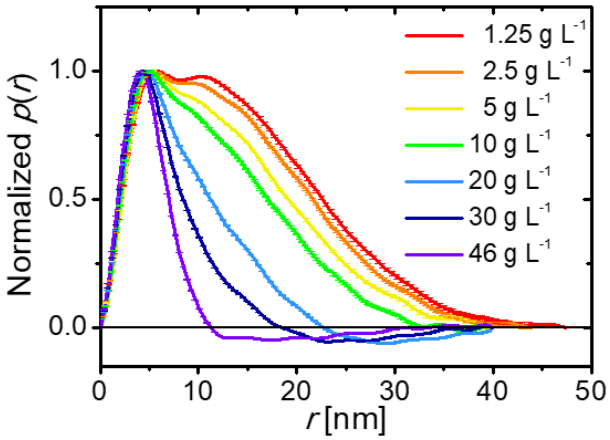

Figure 4. Pair distance distribution functions $p(r)$, normalized to the highest value. The concentrations are given in the graph. The horizontal black solid line indicates $p(r) = 0$.

At concentrations of 10 g L^{-1} and above, $p(r)$ assumes negative values at high distances r, indicating the presence of correlations between the MBs. Thus, in this concentration range, the SAXS data not only contain the form factor scattering of the MBs, but also a structure factor. The higher the concentration, the stronger is its influence. Therefore, a structure factor is included in the model fit in this concentration range (eq 2).

Model Fitting

For model fitting, the form factor of flexible cylinders, $P_{fc}(q)$, was chosen to describe the MBs. It gives the conformational parameters, including the contour length L_c, the persistence length l_p and the cross-sectional radius R_c of the chain-like MBs (eq 1 and eqs S1 and S2 in the SI). For concentrations at and above 10 g L^{-1}, $P_{fc}(q)$ is multiplied with the structure factor of worm-like chains, $S_{wlc}(q)$ (eqs 2 and S3-S6 in the SI). The latter includes the values of L_c and l_p from $P_{fc}(q)$ and thus describes the correlation between the MBs in dependence on their size and shape. From

$S_{wlc}(q)$, an interaction factor β, revealing the interaction strength, and the interaction length L_{int} are obtained. The scattering from the side chains, namely the decay at $q > 1.5$ nm^{-1} for concentrations of 10-46 g L^{-1} (Figure 3), is modeled by the Ornstein-Zernike structure factor, from which the correlation length ξ of the local density fluctuation in the solution is given (eq 2 and eq S7 in the SI). Using these models, excellent fits were obtained (Figure 3 and Figure S3 in the SI).

Dependence of the Form Factor on Concentration

Having fitted the models described above, the form factor of flexible cylinders, $P_{fc}(q)$, can be considered separately (Figure 5a). The crossover from the plateau at low q-values to the decay with $I(q) \propto q^{-5/3}$ moves to higher q-values, as concentration is increased, i.e. the overall size decreases. In contrast, in the high-q region, the curves do not change with concentration, indicating a constant cross-sectional radius R_c.

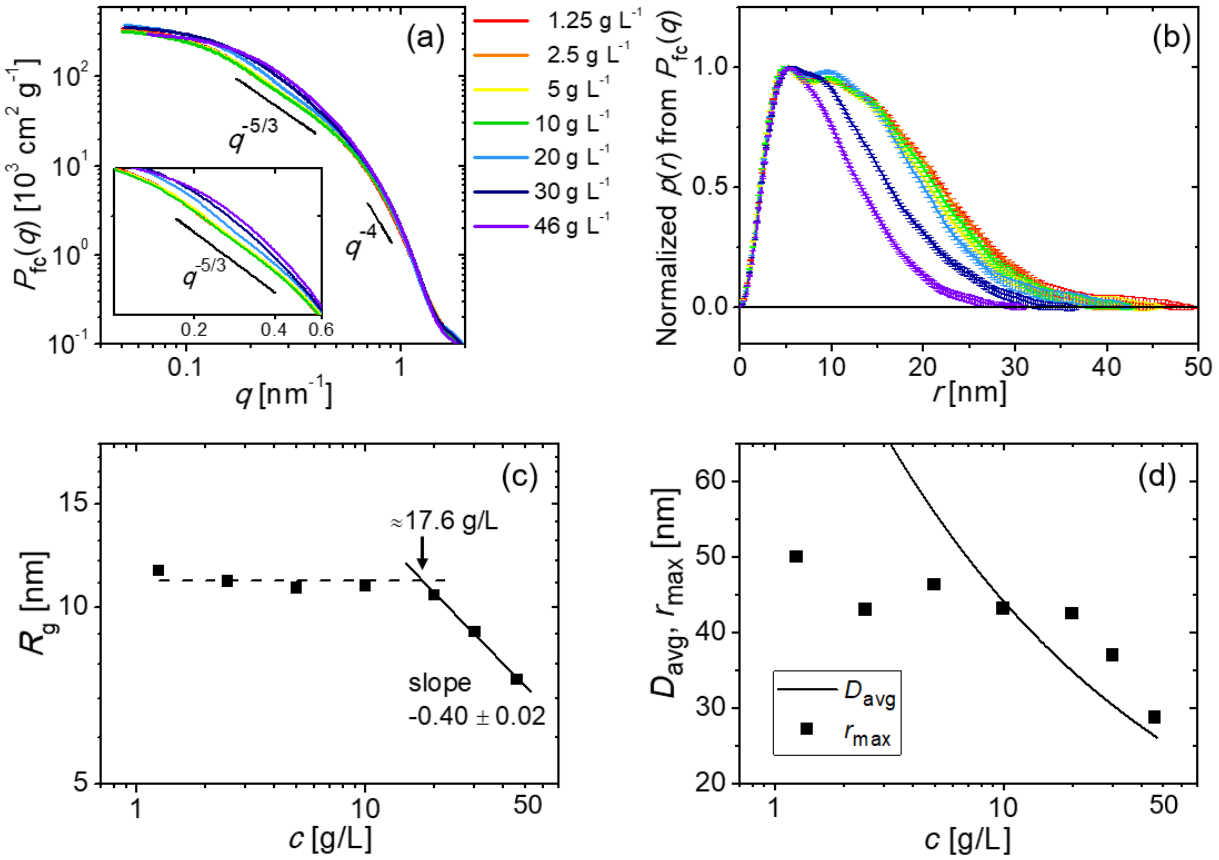

Figure 5. (a) Form factors $P_{fc}(q)$ obtained by model fitting the SAXS data for the concentrations given in the graph. (b) Corresponding pair distance distribution functions, $p(r)$, derived from $P_{fc}(q)$. The curves are normalized to the highest value. The horizontal black solid line indicates $p(r) = 0$. (c) Radius of gyration R_g resulting from $p(r)$ as a function of concentration c. The dashed line is a horizontal regression line from 1.25 to 10 g L^{-1}. The solid line is a linear regression of the data points from 20 to 46 g L^{-1} corresponding to $R_g \propto c^{-0.40\pm0.02}$. (d) Largest dimension within the MBs, r_{max}, as a function of concentration (symbols). Calculated average distance between the MBs, D_{avg} (line).

Calculating the pair distance distribution functions $p(r)$ from these $P_{fc}(q)$ curves (Figure 5b) allows evaluating their shape and size without any influence of the structure factor. Between 1.25 and 20 g L^{-1}, the $p(r)$-functions feature two maxima at $r = 5$ nm and $r = 11$ nm and an asymmetric

overall shape, with the decay at high *r*-values shifting to slightly smaller *r*-values with increasing concentration. From 20 to 46 g L^{-1}, the $p(r)$-functions become steadily less asymmetric, while they shift to substantially smaller *r*-values. The asymmetric shape suggests an overall anisotropic shape of the MBs at all concentrations, and the changes from 1.25 to 46 g L^{-1} indicate a gradual decrease in the geometrical asymmetry of the particle.

Furthermore, *ab initio* shape modeling of the $P_{fc}(q)$ curves allows construction of 3-dimensional models of the MBs at different concentrations, using densely packed beads as the basic constituents. These models give information about the average overall geometry of the MBs. It should be also pointed out that, while the *ab initio* shape modeling is routinely used for the SAS data analysis of biological samples, it has also, more recently, been applied to data from nanoparticles,[58,59,60] soft matter[61] and biological-nanoparticle hybrid systems.[62,63] One may expect that conformational heterogeneity in flexible molecules, such as the MBs, will result in likewise heterogeneous *ab initio* solutions, due to the smearing of the reciprocal space features normally present in more rigid molecules. Nevertheless, models representative of the features common to several shape reconstructions are expected to visualize some of the more noticeable shape characteristics in the SAXS curves.

At 1.25 g L^{-1}, the MBs are composed of about four to five small domains, each 8.0-9.0 nm in size, that are connected like pearls on a string (Figure 6a). Given the rather high flexibility at this concentration, the model clusters exhibit different types of assembly for these domains, as indicated by the NSD values, that vary between 1.1 and 1.5. At 10 g L^{-1}, the MBs maintain their elongated shape, while the individual domains start to become smaller in size (~6.0 nm) and less obvious in the model (Figure 6b). A reduced flexibility of the particle shape can be perceived from a lower NSD value (1.2). At 46 g L^{-1}, the small domains cannot be distinguished from each other

anymore, and the MBs show a compact, flat molecular shape (thickness ~4.5 nm, NSD 0.9-1.3, Figure 6c). Thus, the MBs undergo a shape transformation from 10 to 46 g L^{-1}, becoming more compact and less anisotropic, and these changes can be easily visualized in the *ab initio* models. This result corresponds very well to the observation from the $p(r)$-functions (Figure 5b) and agrees with the findings by Sunday et al.[39]

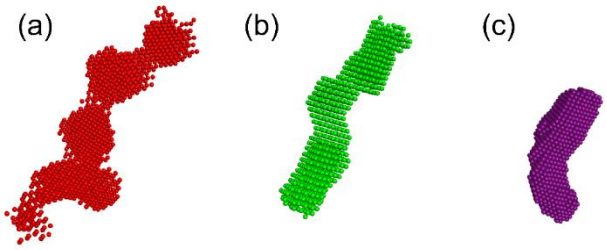

Figure 6. Results from *ab initio* shape modeling of the $P_{fc}(q)$ curves at (a) 1.25 (b) 10 and (c) 46 g L^{-1}.

The radius of gyration of the MBs, R_g, as obtained from the $p(r)$-functions of $P_{fc}(q)$ is shown in Figure 5c in dependence on concentration. While R_g stays at ~11.5 nm between 1.25 and 10 g L^{-1} and barely changes, it decreases with increasing c from 20 to 46 g L^{-1}, following the scaling relation $R_g \propto c^{-0.4}$. The scaling exponent of -0.4 suggests that inter- and intra-side chain interactions between the MBs dominate (regime (4) defined in the simulation study by Paturej and Kreer).[17] Noticeably, neither the scaling regime of the backbone interaction (regime (1)) nor the one of the persistence segments (regime (2)), which would feature exponents of -0.125 and -0.25,[17] are observed in the present system. This behavior may be attributed to the molecular architecture of the MBs under study, that feature densely grafted side chains, which are long enough to affect the overall conformation of the MBs.

The maximum dimension, r_{max}, as obtained from the point where the $p(r)$ functions in Figure 5b become zero, is shown in Figure 5d. Between 1.25 and 20 g L^{-1}, r_{max} decreases slightly from ~50

nm to ~43 nm and then strongly to 29 nm at 46 g L^{-1}. Comparing the values with the average distance between the MBs, D_{avg}:

$$D_{avg}{}^{3} = \frac{M_w}{cN_A} \quad (3)$$

(N_A is Avogadro's constant), that is calculated from the concentration and the corresponding number of MBs per unit volume, it is seen that r_{max} coincides with D_{avg} at ~10 g L^{-1} and becomes larger than D_{avg} at higher concentrations. Namely, the MBs are uncorrelated below 10 g L^{-1}, while they are correlated above. Thus, the overlap concentration may be estimated at c^* = 10 g L^{-1}.

From fitting the described models, a contour length of the MBs, L_c = 56.7 ± 1.5 nm, is obtained at 1.25 g L^{-1}. Meanwhile, the fully extended length of the MB amounts to 66.8 nm, as estimated from the product of (i) the sum of the degrees of polymerization of the backbone and two times the one of the side chains, $N_{bk} + 2N_{sc}$, and (ii) the monomer length, which is calculated from the length of the C-C and C-N chemical bonds and the bond angles.[64] Thus, the experimentally obtained L_c amounts to ~85 % of the fully extended length, implying a rather stretched conformation of the backbone. Since the value of L_c can be expected to be independent on the concentration, L_c = 56.7 nm is used for the model fits at all concentrations.

The resulting persistence length l_p in dependence on c is shown in Figure 7. Between 1.25 and 10 g L^{-1}, it is constant at ~10 nm. This is close to the maximum at $r \cong 11$ nm in the $p(r)$-functions (Figure 5b), and we attribute this maximum to the persistence length of the MBs. Comparing with the l_p value of the bare backbone, namely ~1.5 nm,[65,66] the l_p value of the MB is significantly larger, implying an increase of the backbone rigidity due to the dense grafting of the side chains, which seems plausible. Above 10 g L^{-1}, l_p of the MBs decreases steadily with increasing c, until it reaches a value of 3 nm at 46 g L^{-1}. (We note that the latter value is only slightly larger than the cross-sectional radius, see below, and has to be taken with care.) This means, the MBs become

significantly more flexible, which is supposedly a result of the enhanced mutual interaction between the MBs in this concentration range.[35] Interestingly, the concentration where the interpolated values of l_p cross over, i.e., 17 g L^{-1}, is similar to the one where R_g starts to decrease, namely 20 g L^{-1} (Figure 5c). This again suggests that the rigidity of the MBs starts to weaken at a concentration between 10 and 20 g L^{-1}. Thus, combining both results, we conclude that the overlap concentration c^* of the solution is in the range of 10-20 g L^{-1}.

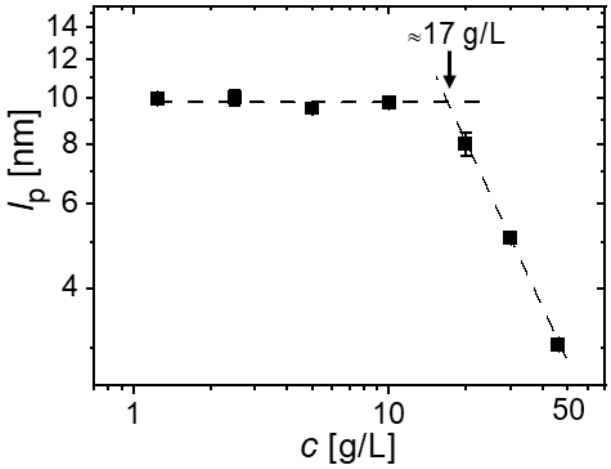

Figure 7. Persistence length l_p from model fitting as a function of concentration c in a double-logarithmic representation. The two dashed lines serve as guides for the eyes. Their crossover is indicated.

In contrast to the overall radius of gyration and the persistence length, which depend on concentration above 10-30 g L^{-1}, the cross-sectional radius R_c fluctuates around 2.5 nm in the entire concentration range without any trend, presumably because of the short side chain length (Figure 8a). The corresponding cross-sectional diameter of 5 nm compares well with the r-value of the first maximum in the $p(r)$-functions, observed for all concentrations (Figure 5b). Thus, the finite cross section of the MB is probably at the origin of the maxima at $r \cong 5$ nm in the $p(r)$-functions. Finally, the correlation length ξ, from the Ornstein-Zernike structure factor, characterizing the

local concentration fluctuations mainly of the side chains at the periphery of the MBs, is found to be ~1 nm (Figure 8b), without any clear dependence on concentration. Thus, neither the cross-sectional radius nor the concentration fluctuations of the side chains change with concentration.

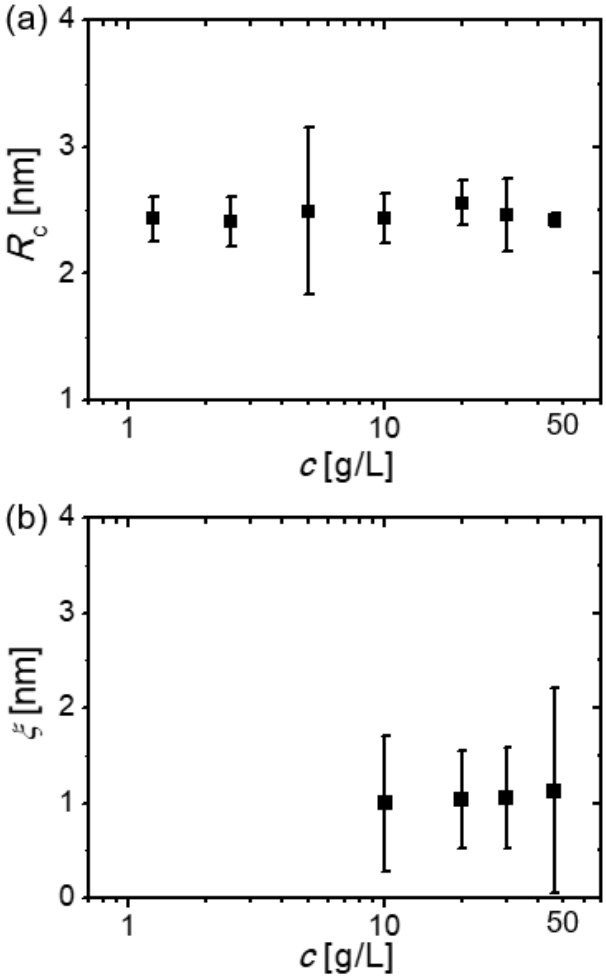

Figure 8. Structural parameters at small length scales in dependence on concentration on a logarithmic scale. (a) Cross-sectional radius R_c from the form factor, (b) correlation length ξ from the Ornstein-Zernike function.

Dependence of the Structure Factor on Concentration

The correlation between the MBs in the solutions having concentrations of 10-46 g L^{-1} is described by the structure factor of worm-like chains, $S_{wlc}(q)$, see eqs 2 and S3-S6 in the SI. $S_{wlc}(q)$ is expressed as a function of the form factor $P_{fc}(q)$ and thus contains the structural parameters L_c and l_p. The parameters from $S_{wlc}(q)$, describing the correlation between the MBs, are L_{int} and β. L_{int} describes the screening for persistence chains that are in solution at intermediate concentrations. The screening is not the same for segments in the center and segments close to the end of the chain. Therefore, the structure factor includes a length scale, that is related to the concentration and the chain length and is called the screening length. β is positively related to the interaction strength between the MBs.

The resulting L_{int} values decrease with increasing concentration (Figure 9a), and the values fall between r_{max} (Figure 5d) and R_c (Figure 8a), corresponding well to the predicted length scale. β increases with increasing concentration (Figure 9b, symbols), reflecting the enhanced interaction strength. Using the relations in eqs S4 and S5 in the SI, assuming c^* = 10 or 17 g L^{-1}, estimates of β in dependence on concentration are obtained (Figure 9b). The experimental data fall between these two theoretical curves, which justifies the validity of $S_{wlc}(q)$ in the MB solutions for concentrations above c^*.

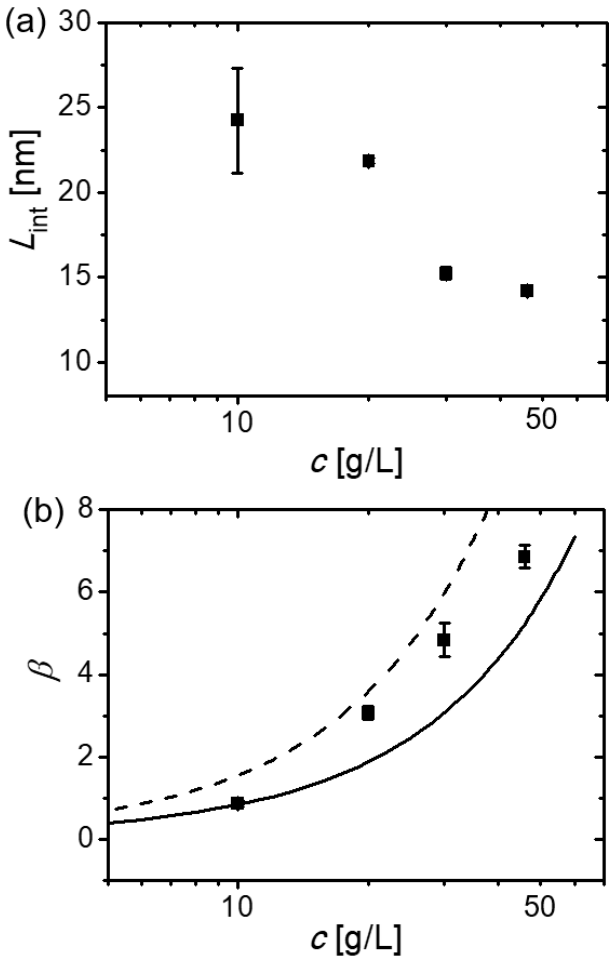

Figure 9. Structural parameters from model-fitting of the structure factor of worm-like chains, $S_{wlc}(q)$, in dependence on concentration on a logarithmic scale. (a) Characteristic interaction length L_{int}. (b) Interaction parameter β (symbols). Calculated β-values, assuming $c^* = 10$ g L^{-1} (dashed line) and $c^* = 17$ g L^{-1} (solid line).

Computer Simulations of Molecular Brush Solutions

Dissipative particle dynamics (DPD) simulations[67,68] were used to study the solutions of branched macromolecules.[69,70] The description of the simulation systems can be found in the SI. The concentration was varied from 0.17 to 5 vol.-%, which corresponds to the experimentally studied concentrations. The results are presented in Figure 10. A visual analysis of the snapshots

(Figure 10a) reveals the following behavior: At low concentrations (c = 0.5-1 %), the brushes prefer to attain an extended worm-like conformation. At intermediate concentrations, the brushes begin to bend (c = 1.5%), which eventually results in the more compact coil-like conformations at higher concentrations (c = 3 and 5 %).

The further quantitative analysis of the brush solutions comprises the calculations of the persistence length l_p^{DPD} (Figure 10b) and the gyration radius R_g^{DPD} (Figure 10c) as a function of the polymer concentration. Here the persistence length was estimated by

$$\langle R^2 \rangle = 2 l_p^{\mathrm{DPD}} L_c^{\mathrm{DPD}} \left[1 - \frac{l_p^{\mathrm{DPD}}}{L_c^{\mathrm{DPD}}} \left(1 - e^{-L_c^{\mathrm{DPD}} / l_p^{\mathrm{DPD}}} \right) \right] \quad (4)$$

where $\langle R^2 \rangle$ is the mean-square end-to-end distance and L_c^{DPD} the contour length of the backbone. In our simulations, the value of L_c^{DPD} remained constant, regardless of polymer concentration, and was equal to 143.6 ± 1.5 nm, which is more than 2 times higher than the value calculated from the $p(r)$-functions. At the same time, as it can be seen in Figures 10b and 10c, the values of l_p^{DPD} and R_g^{DPD} at low concentrations (c = 0.17-1 %) were estimated as ~6 nm and ~14 nm, respectively. Meanwhile, the increase of polymer concentration results in a significant decrease of l_p^{DPD} until the value of 3.5 nm, while the R_g^{DPD} changes only weakly within the considered concentration range (Figure 10b and c). Such quantitative discrepancy with the experimental results (i.e. a less pronounced decrease of l_p^{DPD} and R_g^{DPD}) may be attributed to the assumption of full flexibility of both the backbone and side chains at the selected level of coarse-graining (1 bead equals 1 monomer, see the SI). Nevertheless, the values of l_p^{DPD} at c > 3% matches with the ones obtained from the experiments which confirms the flexible chain behavior of molecular brushes at high polymer concentrations (Figure 7). Other agreement with the experiments can be found for the overlap concentration c^* which is equal to 1.5 % (inflection point in Figure 10b) and lies exactly in the range between 10 g L^{-1} and 17 g L^{-1} (Figure 9b). Finally, the mean brush thickness R_c^{DPD}

was estimated as 4.52 ± 0.06 nm for all concentrations, which also agrees nicely with the constancy of the cross-sectional radius R_c (~2.5 nm, Figure 8a) and may serve as an argument that the P*n*PrOx side chains are more flexible than the initial P*i*POx backbone. In other words, the results of computer simulations show a good correlation with the results SAXS measurements and confirm the proposed behavior of molecular brush solutions.

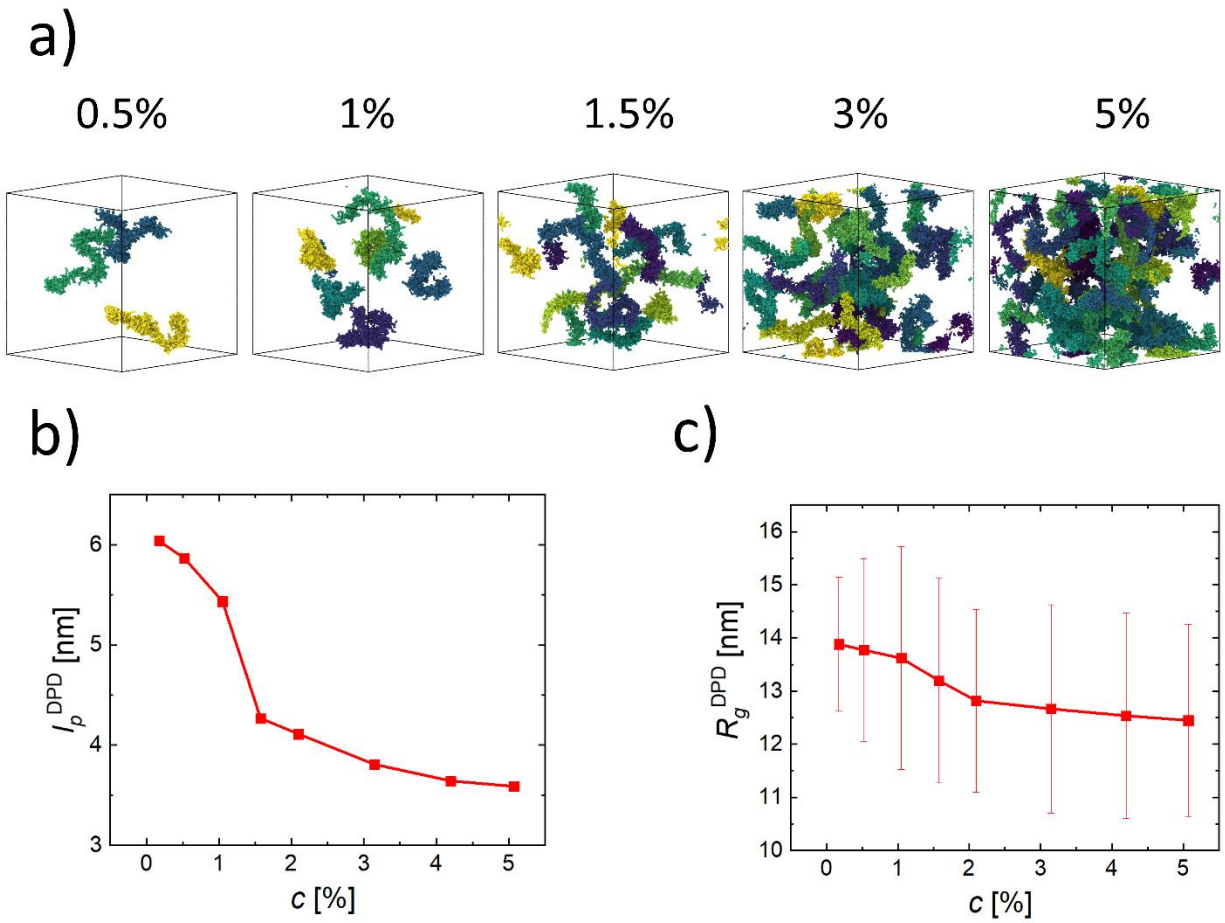

Figure 10. (a) Simulation snapshots of molecular brush solutions at different polymer concentrations (for convenience, the solvent beads are not shown, and each brush is colored individually). (b) Persistence length l_p^{DPD} and (c) radius of gyration R_g^{DPD} as a function of the polymer concentration.

Conclusions

Based on the structural analysis by SAXS and the DPD simulations, the conformational changes of P*i*POx$_{239}$-*g*-P*n*PrOx$_{14}$ in dependence on solution concentration in a good solvent can be sketched, as shown in Figure 11. In dilute solution, these MBs assume an elongated worm-like shape, with the structure being unchanged up to 10 g L^{-1}. As the concentration increases from 20 to 46 g L^{-1}, both the brush size (R_g and r_{max}) and the persistence length l_p decrease steadily with increasing concentration, indicating a reduced backbone rigidity of the MB. Despite these significant changes, the cross section of the MBs and the correlation length of concentration fluctuations within the MBs, which are both related to the densely grafted side chains, maintains their value throughout the entire concentration range.

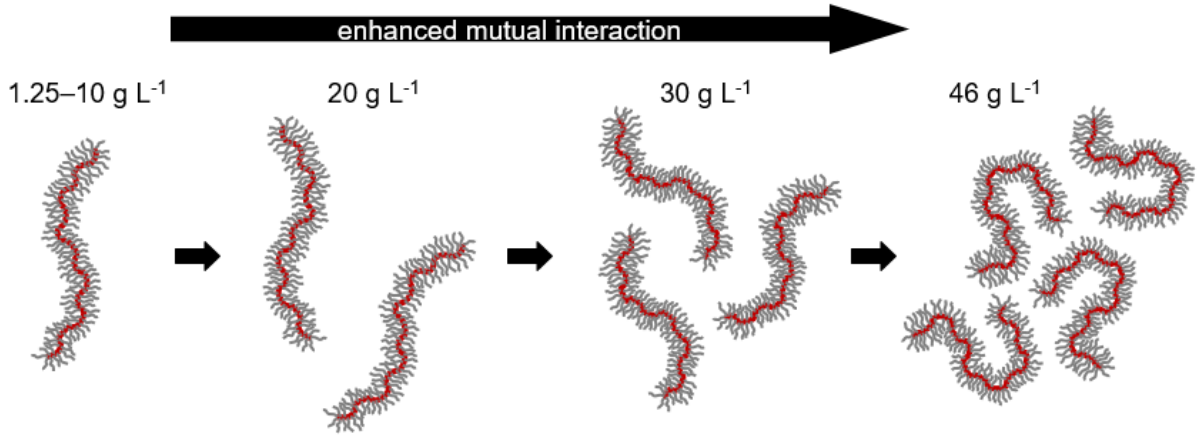

Figure 11. Schematic representation of the structural evolution upon increasing concentration of the chain-like MB P*i*POx$_{239}$-*g*-P*n*PrOx$_{14}$ in a good solvent, ethanol.

From the scaling behavior of the radius of gyration with concentration, it is found that the rigid-to-flexible transition of the backbone is driven by the interaction between the side chains. A direct transition from the non-interacting state ($R_g \propto c^0$) to the side chain interaction state ($R_g \propto c^{-0.4}$) is found, while neither the predicted backbone interaction state nor the predicted persistence length

interaction states are observed. This result is tentatively attributed to the dominant role of the side chains in the architecture of the MB. The exponents identified by us differ from the ones of Bolisetty et al.,[34,35] while there is a certain similarity with the findings of Sunday et al.[39] The reason for these discrepancies may lie in the different ratios of N_{sc} and N_{bk}: The one investigated by us (~17) lies between the ones studied by Bolisetty et al. (~26) and Sunday et al. (2.6).

Our results show in how far the conformation of chain-like MBs deviates from the conformation of linear polymers in dilute and semi-dilute solution and in which way the complex molecular architecture affects the scaling behavior of the overall size with concentration in the semi-dilute regime. Synchrotron small-angle X-ray scattering proved useful to address a wide range of length scales. As for model fitting the SAXS data in terms of a form and structure factor, it proved essential to properly take into account the form factor of the MBs in the expression of the structure factor. In addition, the results from DPD simulations are in good agreement with the SAXS measurements.

ASSOCIATED CONTENT

Supporting Information. The following files are available free of charge.

SEC Elugram of P*i*POx$_{239}$-*g*-P*n*PrOx$_{14}$. Model Functions Used for Fitting of SAXS Data. Example Fits of SAXS Data. SAXS Data Shown as Kratky Plots. Structural Parameters. Confidence Intervals of the Fit Parameters. Dissipative Particle Dynamics (DPD) Simulations. (PDF)

AUTHOR INFORMATION

Corresponding Author

* Christine M. Papadakis, e-mail papadakis@tum.de

Present Addresses

† Jia-Jhen Kang: Jülich Centre for Neutron Science (JCNS) at Heinz Maier-Leibnitz Zentrum, Forschungszentrum Jülich GmbH, Lichtenbergstraße 1, 85748 Garching, Germany

Martin A. Schroer: Nanoparticle Process Technology, University of Duisburg-Essen, Lotharstraße 1, 47057 Duisburg, Germany.

Author Contributions

The manuscript was written through contributions of all authors. All authors have given approval to the final version of the manuscript.

Funding Sources

We thank Deutsche Forschungsgemeinschaft (PA 771/27-1, JO 287/14-1) for funding. S. D. V. acknowledges funding from the Joachim Herz Stiftung (Hamburg, Germany). D. M. acknowledges the BMBF grant 16QK10A (SAS-BSOFT). The computer simulations were performed with financial support of the Russian Foundation for Basic Research, project No. 20-53-12023.

Notes

This paper is dedicated to the late Françoise Winnik.

ACKNOWLEDGMENT

We thank Johannes Allwang (Technical University of Munich, Germany) for initial experiments. Also, we thank Jan Skov Pedersen (Aarhus University, Denmark) for providing help on the interpretation of the SAXS fitting parameters. This work is based upon experiments

performed at the P12 Bio-SAXS instrument operated by European Molecular Biology Laboratory (EMBL), Hamburg Outstation, Deutsches Elektronen-Synchrotron, Germany. EMBL is acknowledged for beam time allocation and for providing excellent equipment. The computer simulations were performed using the equipment of the shared research facilities of HPC computing resources at Lomonosov Moscow State University.[71]

REFERENCES

1. Sheiko, S. S.; Sumerlin, B. S.; Matyjaszewski, K. Cylindrical Molecular Brushes: Synthesis, Characterization, and Properties. *Prog. Polym. Sci.* **2008**, *33*, 759-785.

2. Yuan, J.; Müller, A. H. E.; Matyjaszewski, K.; Sheiko, S. S., 6.06 - Molecular Brushes. In *Polymer Science: A Comprehensive Reference*, Matyjaszewski, K., Möller, M., Eds. Elsevier: Amsterdam, 2012; pp 199-264.

3. Verduzco, R.; Li, X.; Pesek, S. L.; Stein, G. E. Structure, Function, Self-Assembly, and Applications of Bottlebrush Copolymers. *Chem. Soc. Rev.* **2015**, *44*, 2405-2420.

4. Li, Z.; Tang, M.; Liang, S.; Zhang, M.; Biesold, G. V.; He, Y.; Hao, S.; Choi, W.; Liu, Y.; Peng, J.; Lin, Z. Bottlebrush Polymers: From Controlled Synthesis, Self-Assembly, Properties to Applications. *Prog. Polym. Sci.* **2021**, 101387.

5. Denesyuk, N. A. Conformational Properties of Bottle-Brush Polymers. *Phys. Rev. E* **2003**, *67*, 051803.

6. Hsu, H. P.; Binder, K.; Paul, W. How to Define Variation of Physical Properties Normal to an Undulating One-Dimensional Object. *Phys. Rev. Lett.* **2009**, *103*, 198301.

7. Panyukov, S. V.; Sheiko, S. S.; Rubinstein, M. Amplification of Tension in Branched Macromolecules. *Phys. Rev. Lett.* **2009**, *102*, 148301.

8. Borisov, O. V.; Birshtein, T. M.; Zhulina, Y. B. The Temperature-Concentration Diagram of State for Solutions of Comb-Like Macromolecules. *Polym. Sci. (USSR)* **1987**, *29*, 1552-1559.

9. Birshtein, T. M.; Borisov, O. V.; Zhulina, Y. B.; Khokhlov, A. R.; Yurasova, T. A. Conformations of Comb-Like Macromolecules. *Polym. Sci. (USSR)* **1987**, *29*, 1293-1300.

10. Elli, S.; Ganazzoli, F.; Timoshenko, E. G.; Kuznetsov, Y. A.; Connolly, R. Size and Persistence Length of Molecular Bottle-Brushes by Monte Carlo Simulations. *J. Chem. Phys.* **2004**, *120*, 6257-6267.

11. Feuz, L.; Leermakers, F. A. M.; Textor, M.; Borisov, O. Bending Rigidity and Induced Persistence Length of Molecular Bottle Brushes: A Self-Consistent-Field Theory. *Macromolecules* **2005**, *38*, 8891-8901.

12. Yethiraj, A. A Monte Carlo Simulation Study of Branched Polymers. *J. Chem. Phys.* **2006**, *125*, 204901.

13. Hsu, H.-P.; Paul, W.; Binder, K. Structure of Bottle-Brush Polymers in Solution: A Monte Carlo Test of Models for the Scattering Function. *J. Chem. Phys.* **2008**, *129*, 204904.

14. Zhang, Z.; Carrillo, J.-M. Y.; Ahn, S.-k.; Wu, B.; Hong, K.; Smith, G. S.; Do, C. Atomistic Structure of Bottlebrush Polymers: Simulations and Neutron Scattering Studies. *Macromolecules* **2014**, *47*, 5808-5814.

15. Angelescu, D. G.; Linse, P. Monte Carlo Simulations of Multigraft Homopolymers in Good Solvent. *Macromolecules* **2014**, *47*, 415-426.

16. Chatterjee, D.; Vilgis, T. A. Scaling Laws of Bottle-Brush Polymers in Dilute Solutions. *Macromol. Theory Simul.* **2016**, *25*, 518-523.

17. Paturej, J.; Kreer, T. Hierarchical Excluded Volume Screening in Solutions of Bottlebrush Polymers. *Soft Matter* **2017**, *13*, 8534-8541.

18. Dutta, S.; Wade, M. A.; Walsh, D. J.; Guironnet, D.; Rogers, S. A.; Sing, C. E. Dilute Solution Structure of Bottlebrush Polymers. *Soft Matter* **2019**, *15*, 2928-2941.

19. López-Barrón, C. R.; Vargas-Lara, F.; Kang, S. Single-Chain Conformation of Poly(α-olefins) in Dilute Solutions at the Crossover between Linear and Bottlebrush Architectures. *Macromolecules* **2021**, *54*, 6854-6866.

20. Hsu, H.-P.; Paul, W.; Rathgeber, S.; Binder, K. Characteristic Length Scales and Radial Monomer Density Profiles of Molecular Bottle-Brushes: Simulation and Experiment. *Macromolecules* **2010**, *43*, 1592-1601.

21. Rathgeber, S.; Pakula, T.; Wilk, A.; Matyjaszewski, K.; Lee, H.-i.; Beers, K. L. Bottle-Brush Macromolecules in Solution: Comparison between Results Obtained from Scattering Experiments and Computer Simulations. *Polymer* **2006**, *47*, 7318-7327.

22. Rathgeber, S.; Pakula, T.; Wilk, A.; Matyjaszewski, K.; Beers, K. L. On the Shape of Bottle-Brush Macromolecules: Systematic Variation of Architectural Parameters. *J. Chem. Phys.* **2005**, *122*, 124904.

23. Zhang, B.; Gröhn, F.; Pedersen, J. S.; Fischer, K.; Schmidt, M. Conformation of Cylindrical Brushes in Solution: Effect of Side Chain Length. *Macromolecules* **2006**, *39*, 8440-8450.

24. Hsu, H.-P.; Paul, W.; Binder, K. Understanding the Multiple Length Scales Describing the Structure of Bottle-Brush Polymers by Monte Carlo Simulation Methods. *Macromol. Theory Simul.* **2011**, *20*, 510-525.

25. Maleki, H.; Theodorakis, P. E. Structure of Bottle-Brush Brushes under Good Solvent Conditions: A Molecular Dynamics Study. *J. Phys.: Condens. Matter* **2011**, *23*, 505104.

26. Theodorakis, P. E.; Hsu, H.-P.; Paul, W.; Binder, K. Computer Simulation of Bottle-Brush Polymers with Flexible Backbone: Good Solvent Versus Theta Solvent Conditions. *J. Chem. Phys.* **2011**, *135*, 164903.

27. Fredrickson, G. H. Surfactant-Induced Lyotropic Behavior of Flexible Polymer Solutions. *Macromolecules* **1993**, *26*, 2825-2831.

28. Wintermantel, M.; Gerle, M.; Fischer, K.; Schmidt, M.; Wataoka, I.; Urakawa, H.; Kajiwara, K.; Tsukahara, Y. Molecular Bottlebrushes. *Macromolecules* **1996**, *29*, 978-983.

29. Fytas, G.; Nothofer, H. G.; Scherf, U.; Vlassopoulos, D.; Meier, G. Structure and Dynamics of Nondilute Polyfluorene Solutions. *Macromolecules* **2002**, *35*, 481-488.

30. Cheng, G.; Melnichenko, Y. B.; Wignall, G. D.; Hua, F.; Hong, K.; Mays, J. W. Small Angle Neutron Scattering Study of Conformation of Oligo(Ethylene Glycol)-Grafted Polystyrene in Dilute Solutions: Effect of the Backbone Length. *Macromolecules* **2008**, *41*, 9831-9836.

31. Pesek, S. L.; Li, X.; Hammouda, B.; Hong, K.; Verduzco, R. Small-Angle Neutron Scattering Analysis of Bottlebrush Polymers Prepared Via Grafting-through Polymerization. *Macromolecules* **2013**, *46*, 6998-7005.

32. Pesek, S. L.; Xiang, Q.; Hammouda, B.; Verduzco, R. Small-Angle Neutron Scattering Analysis of Bottlebrush Backbone and Side Chain Flexibility. *J. Polym. Sci., Part B: Polym. Phys.* **2017**, *55*, 104-111.

33. Sunday, D. F.; Martin, T. B.; Chang, A. B.; Burns, A. B.; Grubbs, R. H. Addressing the Challenges of Modeling the Scattering from Bottlebrush Polymers in Solution. *J. Polym. Sci.* **2020**, *58*, 988-996.

34. Bolisetty, S.; Airaud, C.; Xu, Y.; Müller, A. H. E.; Harnau, L.; Rosenfeldt, S.; Lindner, P.; Ballauff, M. Softening of the Stiffness of Bottle-Brush Polymers by Mutual Interaction. *Phys. Rev. E* **2007**, *75*, 040803.

35. Bolisetty, S.; Rosenfeldt, S.; Rochette, C. N.; Harnau, L.; Lindner, P.; Xu, Y.; Müller, A. H. E.; Ballauff, M. Interaction of Cylindrical Polymer Brushes in Dilute and Semi-Dilute Solution. *Colloid Polym. Sci.* **2009**, *287*, 129-138.

36. Rosenfeldt, S.; Dingenouts, N.; Ballauff, M.; Lindner, P.; Likos, C. N.; Werner, N.; Vögtle, F. Determination of the Structure Factor of Polymeric Systems in Solution by Small-Angle Scattering: A Sans-Study of a Dendrimer of Fourth Generation. *Macromol. Chem. Phys.* **2002**, *203*, 1995-2004.

37. Rosenfeldt, S.; Karpuk, E.; Lehmann, M.; Meier, H.; Lindner, P.; Harnau, L.; Ballauff, M. The Solution Structure of Stilbenoid Dendrimers: A Small-Angle Scattering Study. *Chemphyschem* **2006**, *7*, 2097-2104.

38. Harnau, L.; Rosenfeldt, S.; Ballauff, M. Structure Factor and Thermodynamics of Rigid Dendrimers in Solution. *J. Chem. Phys.* **2007**, *127*, 014901.

39. Sunday, D. F.; Chremos, A.; Martin, T. B.; Chang, A. B.; Burns, A. B.; Grubbs, R. H. Concentration Dependence of the Size and Symmetry of a Bottlebrush Polymer in a Good Solvent. *Macromolecules* **2020**, *53*, 7132-7140.

40. Kang, J.-J.; Shehu, K.; Sachse, C.; Jung, F. A.; Ko, C.-H.; Barnsley, L. C.; Jordan, R.; Papadakis, C. M. A Molecular Brush with Thermoresponsive Poly(2-ethyl-2-oxazoline) Side Chains: A Structural Investigation. *Colloid Polym. Sci.* **2021**, *299*, 193-203.

41. Zhang, N.; Huber, S.; Schulz, A.; Luxenhofer, R.; Jordan, R. Cylindrical Molecular Brushes of Poly(2-Oxazoline)s from 2-Isopropenyl-2-Oxazoline. *Macromolecules* **2009**, *42*, 2215-2221.

42. Blanchet, C. E.; Spilotros, A.; Schwemmer, F.; Graewert, M. A.; Kikhney, A.; Jeffries, C. M.; Franke, D.; Mark, D.; Zengerle, R.; Cipriani, F.; Fiedler, S.; Roessle, M.; Svergun, D. I. Versatile Sample Environments and Automation for Biological Solution X-Ray Scattering Experiments at the P12 Beamline (Petra III, Desy). *J. Appl. Crystallogr.* **2015**, *48*, 431-443.

43. Round, A.; Felisaz, F.; Fodinger, L.; Gobbo, A.; Huet, J.; Villard, C.; Blanchet, C. E.; Pernot, P.; McSweeney, S.; Roessle, M.; Svergun, D. I.; Cipriani, F. Biosaxs Sample Changer: A Robotic Sample Changer for Rapid and Reliable High-Throughput X-Ray Solution Scattering Experiments. *Acta Crystallogr. D* **2015**, *71*, 67-75.

44. Schroer, M. A.; Blanchet, C. E.; Gruzinov, A. Y.; Gräwert, M. A.; Brennich, M. E.; Hajizadeh, N. R.; Jeffries, C. M.; Svergun, D. I. Smaller Capillaries Improve the Small-angle X-ray Scattering Signal and Sample Consumption for Biomacromolecular Solutions. *J. Synchrotron Radiat.* **2018**, *25*, 1113-1122.

45. Franke, D.; Kikhney, A. G.; Svergun, D. I. Automated Acquisition and Analysis of Small Angle X-Ray Scattering Data. *Nucl. Instrum. Methods Phys. Res* **2012**, *689*, 52-59.

46. Glatter, O., Modern Methods of Data Analysis in Small-Angle Scattering and Light Scattering. In *Modern Aspects of Small-Angle Scattering*, Brumberger, H., Ed. 1995; pp 107-180.

47. Konarev, P. V.; Volkov, V. V.; Sokolova, A.V.; Koch, M. H. J.; Svergun, D. I. PRIMUS - A Windows-PC Based System for Small-angle Scattering Data Analysis. *J. Appl. Crystallogr.* **2003**, *36*, 1277-1282.

48. Franke, D.; Svergun, D.I. DAMMIF, a Program for Rapid ab-initio Shape Determination in Small-angle Scattering. *J. Appl. Crystallogr.* **2009**, *42*, 342–346.

49. Petoukhov, M. V., Franke, D., Shkumatov, A. V., Tria, G., Kikhney, A. G., Gajda, M., Gorba, C., Mertens, H. D. T., Konarev, P. V.; Svergun, D. I. New Developments in the ATSAS Program Package for Small-angle Scattering Data Analysis. *J. Applied Crystallogr.* **2012**, *45*, 342-350.

50. Kozin, M.B.; Svergun, D.I. Automated Matching of High- and Low-resolution Structural Models. *J. Applied Crystallogr.* **2001**, *34*, 33-41.

51. Manalastas-Cantos, K.; Konarev, P. V.; Hajizadeh, N. R.; Kikhney, A. G.; Petoukhov, M. V.; Molodenskiy, D. S.; Panjkovich, A.; Mertens, H. D. T.; Gruzinov, A.; Borges, C.; Jeffries, C. M.; Svergun, D. I.; Franke, D. ATSAS 3.0: Expanded Functionality and New Tools for Small-Angle Scattering Data Analysis. *J. Appl. Crystallogr.* **2021**, *54*, 343-355.

52. Pedersen, J. S.; Schurtenberger, P. Scattering Functions of Semiflexible Polymers with and without Excluded Volume Effects. *Macromolecules* **1996**, *29*, 7602-7612.

53. Chen, W.-R.; Butler, P. D.; Magid, L. J. Incorporating Intermicellar Interactions in the Fitting of Sans Data from Cationic Wormlike Micelles. *Langmuir* **2006**, *22*, 6539-6548.

54. Pedersen, J. S.; Schurtenberger, P. Scattering Functions of Semidilute Solutions of Polymers in a Good Solvent. *J. Polym. Sci., Part B: Polym. Phys.* **2004**, *42*, 3081-3094.

55. Shibayama, M.; Tanaka, T.; Han, C. C. Small Angle NeutronScattering Study on Poly(*N*-isopropyl acrylamide) Gels Near their Volume-Phase Transition Temperature. *J. Chem. Phys.* **1992**, *97*, 6829-6841.

56. Bressler, I.; Kohlbrecher, J.; Thunemann, A. F. Sasfit: A Tool for Small-Angle Scattering Data Analysis Using a Library of Analytical Expressions. *J. Appl. Crystallogr.* **2015**, *48*, 1587-1598.

57 . Mortensen, K., Structural Studies of Polymer Systems Using Small-Angle Neutron Scattering. In *Advanced Functional Molecules and Polymers Vol 2: Processing and Spectroscopy*, Nalwa, H. S., Ed. Gordon & Breach Science Publ.: 2001; pp 223-269.

58. Gdovinova, V.; Schroer, M.A.; Tomasovicova, N.; Appel, I.; Behrens, S.; Majorosova, J.; Kovac, J.; Svergun, D.I.; Kopcansky, P. Structuralization of Magnetic Nanoparticles in 5CB Liquid Crystals. *Soft Matter* **2017**, *13*, 7890–7896.

59. Sun, Y.; Zuo, X.; Sankaranarayan, S.K.; Peng, S.; Narayan, B.; Kamath, G. Quantitative 3D Evolution of Colloidal Nanoparticle Oxidation in Solution. *Science* **2017**, *356*, 303–307.

60. Luo, Z.; Marson, D.; Ong, Q. K.; Loiudice, A.; Kohlbrecher, J.; Radulescu, A.; Krause-Heuer, A.; Darwish, T.; Balog, S.; Buonsanti, R.; Svergun, D. I.; Posocco, P.; Stellaci, F. Quantitative 3D Determination of Self-assembled Structures on Nanoparticles Using Small Angle Neutron Scattering. *Nature Commun.* **2018**, *9*, 1343.

61. Filippov, S. K.; Franklin, J. M.; Konarev, P. V.; Chytil, P.; Etrych, T.; Bogomolova, A.; Dyakonova, M.; Papadakis, C. M.; Radulescu, A.; Ulbrich, K.; Štěpánek, P.; Svergun, D. I. Hydrolytically Degradable Polymer Micelles for Drug Delivery: A SAXS/SANS Kinetic Study. *Biomacromolecules* **2013**, *14*, 4061-4070.

62. Majorošová, J.; Schroer, M.A.; Tomašovičová, N.; Batková, M.; Hu, P.-S.; Kubovčíková, M.; Svergun, D.I.; Kopčanský, P. Effect of the concentration of protein and nanoparticles on the structure of biohybrid nanocomposites. Biopolymers 2020, 111, e23342.

63. Schroer, M. A.; Hu, P.-S.; Tomasovicova, N.; Batkova, M.; Zakutanska, K.; Wu, P.-Y.; Kopcansky, P. Dependence of the Nanoscale Composite Morphology of Fe_3O_4 Nanoparticle-Infused Lysozyme Amyloid Fibrils on Timing of Infusion: A Combined SAXS and AFM Study. *Molecules* **2021**, *26*, 4864(1-17).

64. Tewari, K. S.; Vishnoi, N. K. *A Textbook of Organic Chemistry*, 4th Ed. Vikas Publsihing House PVT LTD, Noida, India: 2017, ch. 4, p. 50.

65. Amirova, A. I.; Golub, O. V.; Kirila, T. U.; Razina, A. B.; Tenkovtsev, A. V.; Filippov, A. P. Influence of Arm Length and Number on Star-Shaped Poly(2-Isopropyl-2-Oxazoline) Aggregation in Aqueous Solutions near Cloud Point. *Soft Mater.* **2016**, *14*, 15-26.

66. Grube, M.; Leiske, M. N.; Schubert, U. S.; Nischang, I. POx as an Alternative to PEG? A Hydrodynamic and Light Scattering Study. *Macromolecules* **2018**, *51*, 1905-1916.

67. Hoogerbrugge, P. J.; Koelman, J. M. V. A. Simulating Microscopic Hydrodynamic Phenomena with Dissipative Particle Dynamics. *Europhys. Lett.* **1992**, *19*, 155–160.

68. Groot, R. D.; Warren, P. B. Dissipative Particle Dynamics: Bridging the Gap Between Atomistic and Mesoscopic Simulation. *J. Chem. Phys.* **1997**, *107*, 4423–4435.

69. Dockendorff, J.; Mourran, A.; Gumerov, R. A.; Potemkin, I. I.; Möller, M.; Gauthier, M. Metal Coordination Induces Phase Segregation in Amphipolar Arborescent Copolymers with a Core–Shell–Corona Architecture. *Macromolecules* **2020**, *53*, 8108-8122.

70. Gumerov, R. A.; Potemkin, I. I. Computer Simulations of Comb-like Macromolecules with Responsive Diblock Copolymer Side Chains. *Colloid Polym. Sci.* **2021**, *299*, 407–418.

71. Voevodin, V. V.; Antonov, A. S.; Nikitenko, D. A.; Shvets, P. A.; Sobolev, S. I.; Sidorov, I. Yu.; Stefanov, K. S. Voevodin, V. V.; Zhumatiy, S. A. Supercomputer Lomonosov-2: Large Scale, Deep Monitoring and Fine Analytics for the User Community. *Supercomput. Front. Innov.* **2019**, *6*, 4–11.